Reinforced SIL-1 micromembranes integrated on chip. Application to CO_2 separation

I. Pellejero[1], M.A. Urbiztondo[1,2], M.P. Pina[1,3,*], J. Santamaría[1,3,*]

[1]NanoscienceInstitute of Aragón (INA); University of Zaragoza; Edif. I+D+i, Campus Rio Ebro, c/Mariano Esquillor s/n, 50018 Zaragoza, Spain.

[2] Centro Universitario de la Defensa, Academia General Militar, 50090 Zaragoza, Spain

[3]Networking Research Center on Bioengineering, Biomaterials and Nanomedicine, CIBER-BBN, 50018Zaragoza, Spain

Corresponding Authors: tel. +34 976 761155, fax. +34 976 762142 e-mail: mapina@unizar.es; jesus.santamaria@unizar.es

Abstract

A novel 4-step microfabrication process is proposed in this work to prepare arrays of c-oriented silicalite (SIL-1) micromembranes on customized silicon nitride (Si_3N_x) microsieves. The arrays are integrated on chip and their overall porosity values can be tuned from 1.6% to 19.9%. A low stress Si_3N_x microfabricated sieve has been used as support to reinforce via mechanical interlocking and to reduce the effects of the residual stress during membrane processing. The secondary hydrothermal growth over the Si_3N_x microsieves also changes the SIL-1 chemistry, improving its affinity towards CO_2 adsorption. As a result, the SIL-1/Si_3N_x micromembranes integrated on chip facilitate the preferential permeation of CO_2 in CO_2/H_2 mixtures, showing a maximum CO_2/H_2 separation factor of 16.9 and a CO_2 permeance of $8.2 \cdot 10^{-7}$ $mol \cdot m^{-2} \cdot s^{-1} \cdot Pa^{-1}$ at ambient conditions.

Keywords: silicon nitride microsieves, silicalite micromembranes, residual stress, adsorption affinity, carbon dioxide separation.

Graphical Abstract

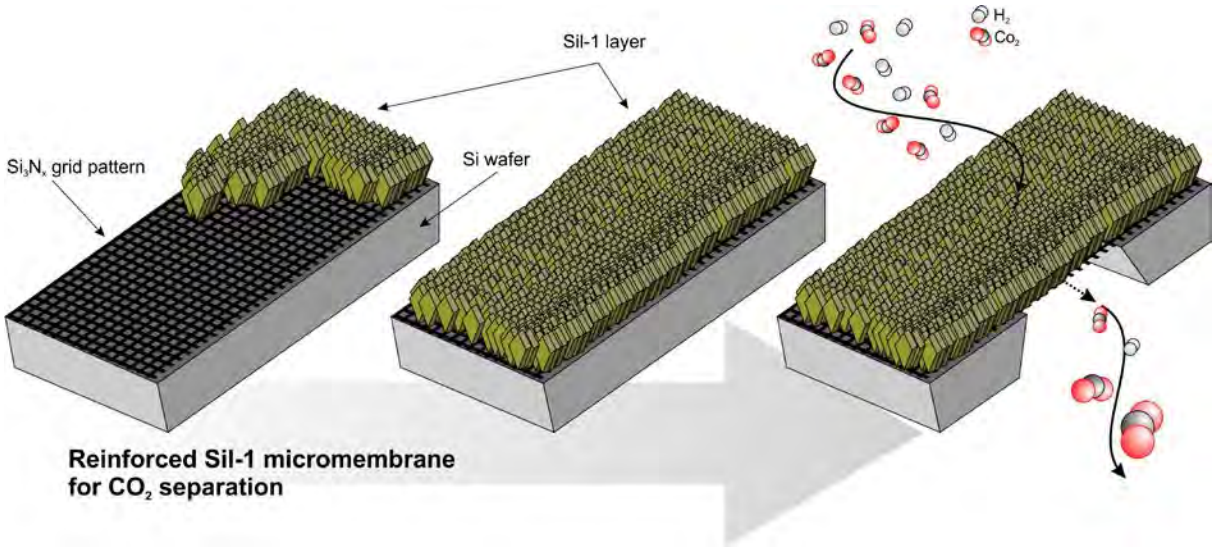

1. Introduction

It is generally accepted that chemical process miniaturization offers important advantages over macroscopic systems regarding the improvement of mass and heat transfer rates, as well as flow and temperature distributions [1]. Additional advantages often quoted for microsystems are low energy consumption, high surface to volume ratio, short response times, safer operation, portability and low unit cost. Also, the advances achieved in silicon, glass and metal processing can often be adapted for mass production of microsystems. However, while relatively simple microstructures (e.g. channels, junctions, micromixers) are amenable for miniaturization, the fabrication of more sophisticated architectures is often challenging. Micro-membranes constitute a clear example of the latter: in this case, a separation layer, with strictly controlled characteristics to achieve permselectivity, must be synthesized or deployed over a microfabricated structure. In spite of the difficulties involved, there is considerable interest in the development of micromembranes because of their broad range of applications including nano-microfiltration, atomization, cross-flow emulsification, controlled drug delivery, optics and photonics, sensors, catalysis and gas separation [2-9].

Despite the intense research efforts on zeolite membranes for energy-intensive industrial separations, several factors including difficulties in scale up are hindering their great potentialities [7, 9-10]. In many cases miniaturization alleviates the problems that appear in the synthesis of large inorganic membranes. It is well-known that the lattice parameters variation of the zeolite crystals upon template removal, along with the mismatch of thermal expansion coefficients between zeolite films and supports [11-15], may result in tensile or compressive stress. Thus, these tensions are imposed on the layer and give rise to crack formation during handling and packaging, or temperature cycling often required for membrane preparation and separation. Actually, scaling-down should allow preparing defect-free zeolite membranes (eventually single crystal membranes) over an endless variety of supports, and combinations with other materials at the micro scale [7] that would have a higher chance for stress tolerance (a very important subject for industrial implementation of this technology). For a given membrane thickness, as permeable area is reduced, the grain boundary characteristics of the zeolite film are improved, i.e. number of extrazeolitic pores is lower [8-9]. In addition, the tensile stress for membrane burst (inversely proportional to permeable area) also increases.

Also, scaling-down makes it possible the preparation of self-supported micromembranes, whose permeance would be enhanced since the mass transfer resistances

attributed to the support can be avoided [16]. Previous attempts to develop zeolite micromembranes have been mostly related to MFI type zeolites, either pure siliceous such as silicalite, denoted as SIL-1 for the remainder of this work, or ZSM-5 with Al in the MFI framework. Up to now, the preparation of zeolite micromembranes has generally followed one of two approaches. Silicalite micromembranes were synthesized on 75 μm thick laser-perforated stainless steel sheets using a seeded growth method [17-18]. In this way, a method to obtain permselective membranes on 75 micron thick stainless steel sheets was obtained. However, the synthesis method used filled most of the support thickness with multiple layers of zeolite crystals, producing relatively thick membranes with reduced permeation. Alternatively, by adapting standard Si based technologies, den Exter et al. [19] in the mid 1990s pioneered the microfabrication process for nonsupported layers of preferential "a" and "b" oriented MFI on silicon/silicon nitride composites. Afterwards, Yeung et al. developed different methods for incorporating zeolite layers onto microchemical systems and microchannels etched on Si wafers for reaction and separation applications [20-24].These authors reported a novel manufacturing process [22-24] for 1 chip containing up to 49 self-standing 5 μm thick MFI micromembranes each with an area of 260x260 μm^2. A clear advantage of this method was the reduced thickness of the self-standing membranes, enabling in principle higher permeation fluxes. On the other hand, the main problem with this approach is the fragility of the membranes produced, which is an inherent characteristic of thin, self-supported polycrystalline zeolite membranes. This limits the dimensions of the free-standing membranes that can be produced, effectively reducing the permeation area.

The aim of this work is the fabrication of defect-free "c" oriented SIL-1 zeolite micromembranes at 3" Si wafer level with good CO_2/H_2 permselectivity. Based on den Exter approach [19], we have carried out the hydrothermal synthesis of SIL-1 micromembranes by secondary growth over customized silicon nitride microsieves. To address the fragility problem mentioned, we firstly fabricated microsieves from low-stress silicon nitride Si_3N_x thin layers grown by LPCVD to be deployed as structural reinforcement for the SIL-1 micromembranes grown on top. Such a stress-free behavior allowed the development of composite structures with minimal internal stress [19] and permeable area higher than those previously reported [23]. Besides, we show that the Lewis base character of the supporting Si_3N_xmicrosieve, capable of partial dissolution during the hydrothermal synthesis of the SIL-1 membrane, enhances the CO_2 separation properties of the resulting micromembranes. We first describe the overall fabrication process for SIL-1 micromembranes over Si_3N_x

microsieves and present its morphological characterization with especial attention to the development of the silicon nitride grid to obtain the desired benefits in terms of reduction in residual stress effects and avoidance of cracks as the permeable area increases. The second part of this work is devoted to the study of the CO_2/H_2 gas separation properties for the selected SIL-1/Si_3N_x micromembranes and performance comparison with published data. The influence of the underlying silicon nitride microsieves over the SIL-1 chemistry and its enhanced affinity towards CO_2 adsorption is also addressed.

2. Experimental

2.1. Materials and Methods

Colloidal silicalite to be used as zeolite seeds was prepared by a hydrothermal route using a solution with the following composition 408 H_2O; 25 TEOS (Tetraethyl orthosilicate) (Aldrich); 9 TPAOH (Tetrapropylammonium hydroxide) (Aldrich); 100 EtOH; according to the recipe of Mintova et al [25]. The resulting product was thoroughly washed with distilled water until pH<8 by repeated cycles of dispersion by ultrasonication and ~~and~~ separation by centrifugation at 9000 rpm. Finally, the seeding suspensions were prepared by dispersing the freshly centrifugated 90 nm discrete SIL-1 nanoparticles in ethanol (99.5% Panreac). A 4 wt% suspension of SIL-1 nanocrystals was used for seeding by spin coating [26-27] on 3'' Si wafers with a low-stress LPCVD silicon nitride (Si_3N_x) layer (1 μm thick) on both sides. On stoichiometric silicon nitride (Si_3N_4) a tensile stress is imposed due to the silicon substrate. Therefore low-stress nitride (Si_3N_x) was used for the purposes of this work.

Hydrothermal synthesis was carried out in a Teflon-lined autoclave (400 mL) for 72 h at 130°C by immersing the pre-seeded wafer into a precursor gel with following molar composition: 2 TPAOH (Tetrapropylammonium hydroxide) (Aldrich); 40 TEOS (Tetraethyl orthosilicate (Aldrich); and 20000 H_2O. The wafer was placed horizontally in a Teflon holder with the seeded surface facing downward at a fixed position to prevent deposition of particles nucleated in the bulk of the solution during synthesis. After the secondary growth, the reaction was quenched to room temperature, and the silicon supports were rinsed vigorously with deionized water and dried at room temperature overnight.

The morphology of the as prepared samples were examined by field emission scanning electron microscopy (FE-SEM), operating at 20 keV (FEI Inspect F). XRD analyses were performed to confirm the purity of the synthesized zeolite membranes.

Gas permeation experiments [28] were performed in a continuous flow mode using a commercial stainless steel filter holder (Pall Corporation PN1209), with an equimolar mixture of carbon dioxide and hydrogen (10 sccm) on the feed (retentate) side of the permeation cell. Ar sweep gas was fed to the permeate side at the same flowrate. The total pressure was maintained at atmospheric value on both sides of the membrane ($\Delta P_{total}=0$). The permeate and retentate compositions were analyzed by on-line gas chromatography (microGC Varian 4900) equipped with two modules (comprising thermal conductivity detector and separation column each one): CP740148 MS5A using Ar as carrier for the analysis of H_2 and CP740150 PPQ using He as carrier for the analysis of CO_2, respectively.

2.2. Fabrication of SIL-1 micromembranes: process definition and morphological characterization

The micromembrane fabrication scheme involves 4 basic steps (A to D) comprising photolithographic and etching processes. The experimental procedure is schematically depicted in Figure 1. Si wafers 3" in diameter, 380±20 μm thickness, <100> orientation, "n" doped and resistivity of 5-10 Ω·cm with a low-stress LPCVD silicon nitride layer (1 μm thick) on both sides were supplied by Siltronix AG. First, a conventional photolithography process was carried out on the backside (resist TI35ES Microchemicals) to define windows on the back Si_3N_x layer (step A) by SF_6 assisted reactive ion etching (RIE). The patterns so defined will determine the permeation area after the final membrane release obtained through backside Si etching (step D). The characteristic dimensions for the different back-side square-shaped designs, given in figure 1 (step A), are the following: 5 mm (type A), 2 mm (type B), 1 mm (type C), 0.83 mm (type D), and 0.7 mm (type E). The photoresist was stripped from the surface using acetone under sonication. Afterwards, a second photolithography process was performed on the front Si_3N_x layer (step B) after proper alignment with the nitride windows defined on the back side (SÜSS MICROTEC MA6). The top side Si_3N_x layer contains circular (d=60 μm) or square (L=200 μm) shaped apertures (see figure 1, step B). These designs allow to obtain porosity values for the Si_3N_x grid (denoted as ε for the remainder of this work) of 57% and 83% respectively. From this point, two different procedures were used, according to the RIE exposure time that resulted in different etching depths. By using "Procedure 1" (3 min RIE time), the resist patterns were only transferred to the Si_3N_x layer. On the other hand, in "Procedure 2" (5 min RIE) RIE time was sufficient to extend etching beyond the Si_3N_x layer to the bulk Si underneath. Since the zeolite membrane

grows on the top surface after etching (step C), by tuning the RIE exposure time, the morphology and microstructure of the resulting membrane could be altered, from which different membrane properties could be expected. Prior to step C (SIL-1 membrane synthesis) the Si wafers were immersed in HF (49% Aldrich) during 30 min for exhaustive cleaning and then in double-distilled water (DDW).

The micromembranes prepared in this work (see Table 2) have been denoted with a three letter code to indicate: i) the back side design with the first letter (A,B,C, D or E); ii) the front side design with the second letter (C or S for circular of square shaped holes in the Si_3N_x microsieve); and iii) the RIE procedure with the third letter (S or L for shorter (Procedure 1) or longer (Procedure 2) respectively.

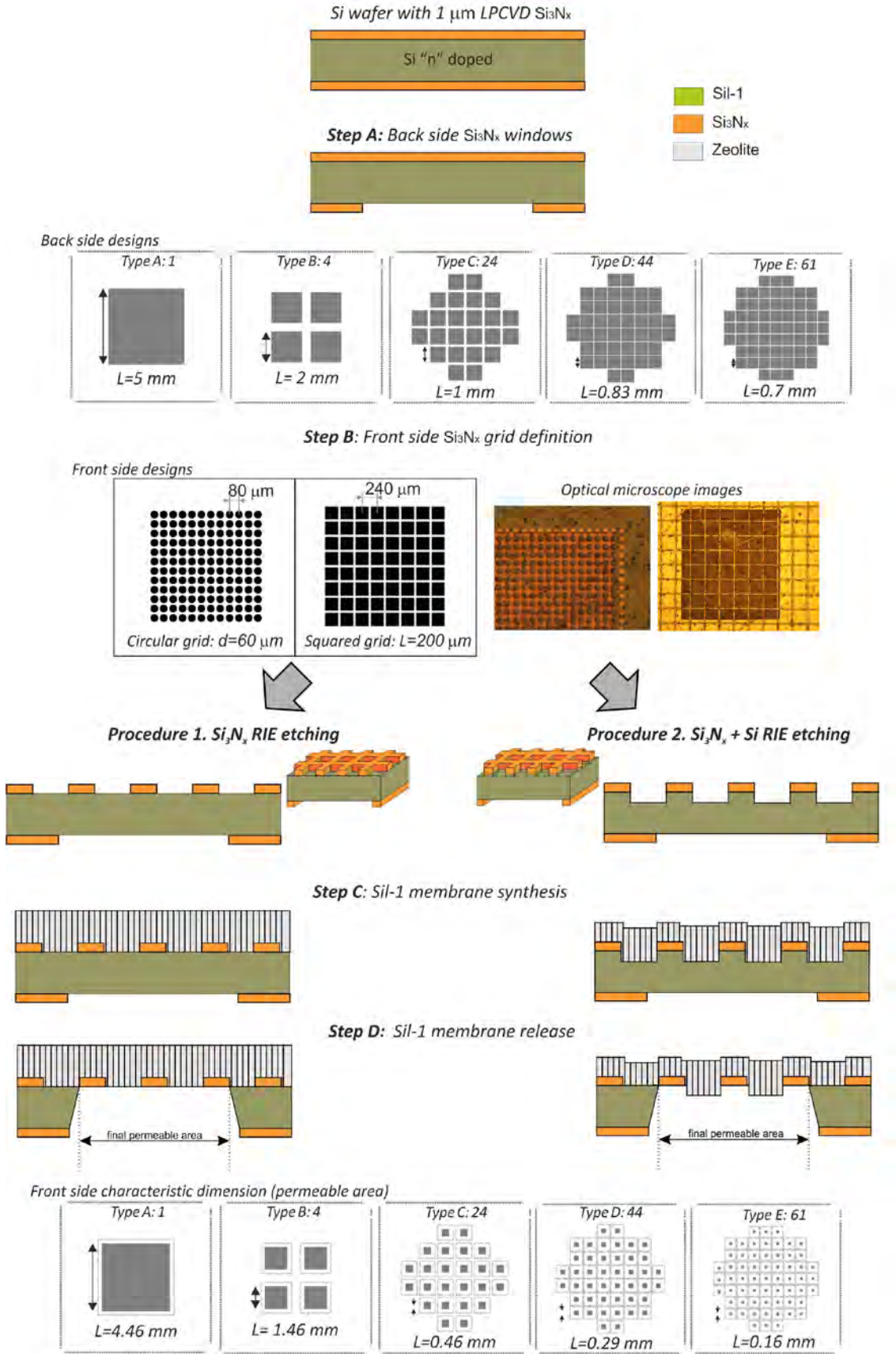

Figure 1. General fabrication scheme for reinforced SIL-1 micromembranes over Si_3N_x microsieves.

”C”-oriented silicalite (SIL-1) polycrystalline layers were synthesized at wafer level (see Figure 2) by secondary (seeded) growth (step C) on the front side of the microfabricated Si wafer according to the procedures already described in previous works [26-27].

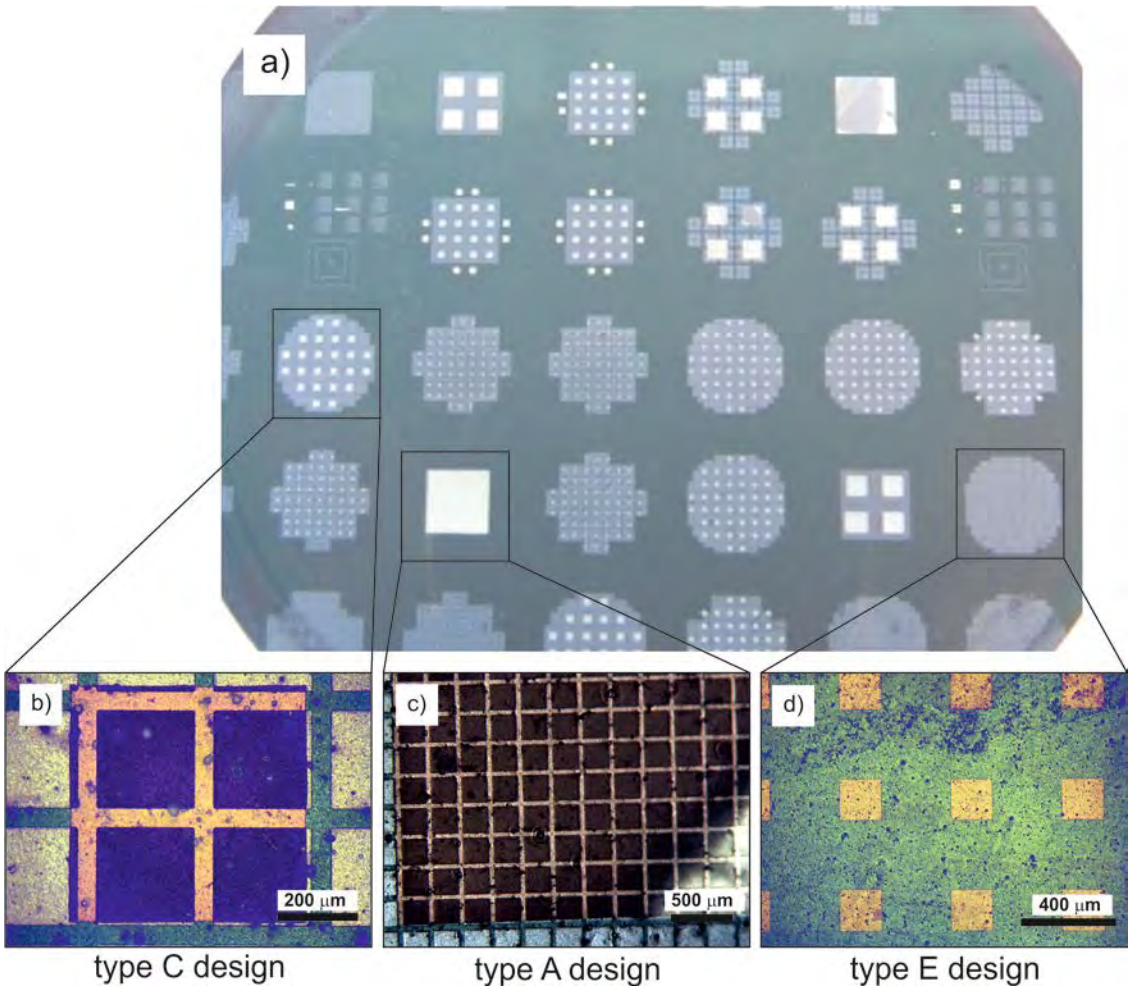

Figure 2. General top view of the different SIL-1/Si_3N_x micromembrane designs patterned on a 3” Si wafer.

Finally, in step (D) the micromembranes are released from the back side by anisotropic bulk Si etching, using a decreasing etching strength first in KOH (20% wt Aldrich) at 70°C followed by TMAH (Tetramethilamonium hydroxide) (25% wt Aldrich) at 80°C [26]. This step was performed at the same time on the whole 3" wafer using a special PEEK holder Single3® with backside and edge protection purchased from AMMT (www.ammt.com). After thoroughly washing with DDW, the Si wafer was removed from the holder and dried in an oven at 100°C for 12 h; then, it was diamond-cut into (1cm x 1cm) slabs for permeation tests.

SEM views of the cross section, and the front and back side views of different types of as prepared SIL-1 micromembranes are shown in Figure 3. It should be pointed out that, because of the anisotropic Si etching, the walls of the etched surfaces are slanted (ϕ= 54.74º), and therefore the area available for permeation is considerably smaller than the windows defined at the back side of the wafer (see Figure 3 a-c and also the scheme in Figure 1). SIL-1 growth was very homogenous, producing membranes with a thickness of 4 ± 0.5 μm that follow the underlying microstructure (see Figure 3 e-i). This behaviour is particularly noticeable for samples prepared according to Procedure 2, where extended RIE conditions provoke 4 μm Si etching. In spite of this, smooth edges are observed for the so obtained terraces (see Figure 3 f), due to negligible under-etching phenomena. In principle, by allowing zeolite growing into the windows of the Si_3N_x microsieves, improved stability could be expected through mechanical interlocking.

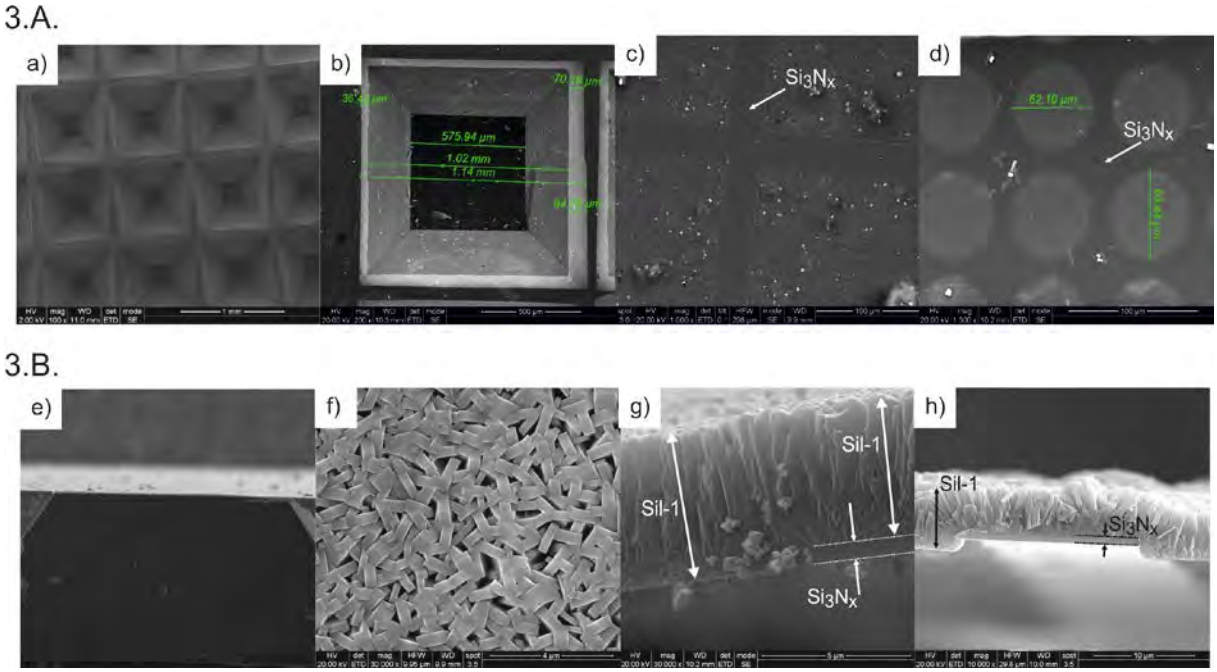

Figure 3. SEM images of the SIL-1 micromembranes prepared in this work (after the step D, silicon release). Back side view for: type D design (a); type C design (b); cross section view for type D design (c); close up view of the top surface (d); cross section view for samples prepared according to Step B: procedure 1. (e); and procedure 2. (f); back side view for samples prepared according to Step B procedure 1: square shaped Si_3N_x grid (g); circular Si_3N_x grid (h); back side view for samples prepared according to Step B procedure 2 circular Si_3N_x grid (i).

3. Results and discussion

3.1. Synthesis of "c" oriented SIL-1 micromembranes over Si_3N_x microsieves

Despite working at the microscale provides a higher chance of tolerating the tensile stresses produced during thermal cycling and calcination of micromembranes, "c" oriented MFI membranes are subjected to severe internal stresses. The randomly oriented seeds deposited on the Si based support, grow in a columnar fashion towards the membrane surface during the hydrothermal synthesis. The competitive growth of the randomly oriented grains results in very homogeneous "c" oriented continuous membrane of large, well-intergrown crystal grains at the membrane surface. In general, the size and orientation of the grain and grain boundary structures have great implications on their mechanical stability. Such intercrystalline pores are unavoidable during hydrothermal synthesis, but some improvement could be performed by optimization of synthesis method [29-30] or post-synthetic treatment, i.e. rapid thermal processing [14-15]. In this work we have developed a silicon nitride grid as a support structure with the aim of attaining more robust c-oriented SIL-1 membranes. Their purity and "c" orientation are confirmed by XRD analysis (see Figure 4). As it can be observed, the XRD pattern of the synthesized micromembranes clearly contains the (002), (012), (103) and (014) diffraction lines of the SIL-1 with c-axis crystallographic preferential orientation. In order to assess the benefits obtained by the deployment of the Si_3N_x grid as a micromembrane support, we compared the SIL-1 micromembranes obtained with another set prepared with a similar microfabrication scheme but without the silicon nitride grid. To this end, step B (grid definition) was not carried out, and instead an additional phosphoric acid (85% wt) etching step at 180ºC was performed just after bulk Si etching (step D) to ensure a complete removal of the exposed Si_3N_x.

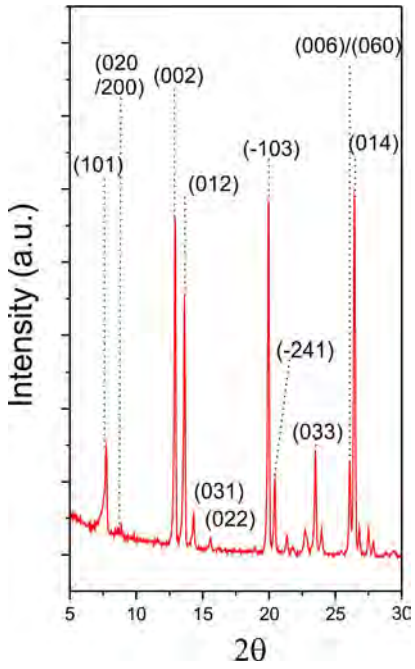

Figure 4. XRD analyses for the SIL1/Si_3N_x micromembranes prepared in this work.

The integrity of the membranes after the microfabrication process was assessed first by inspection using optical microscopy (which also allowed to check the micromembrane characteristic dimension, denoted as w_o), see Figure 2, and also by measuring gas tightness under a 0.2-2 bar trans-membrane pressure difference, depending on membrane design. SEM images for representative examples of different micromembrane designs are compiled in Figure 3. For the gas tightness and permeation measurements each micromembrane chip was glued to a stainless steel circular plate (25 mm diameter) with a central opening (5 mm diameter), then the disk with the micromembranes was mounted in a commercial stainless steel filter holder (Pall Corporation PN1209) as depicted in Figure 5. It is worth mentioning that the gluing and mounting process had to be done with great care to avoid damaging the 4 micron thick membrane layer during handling.

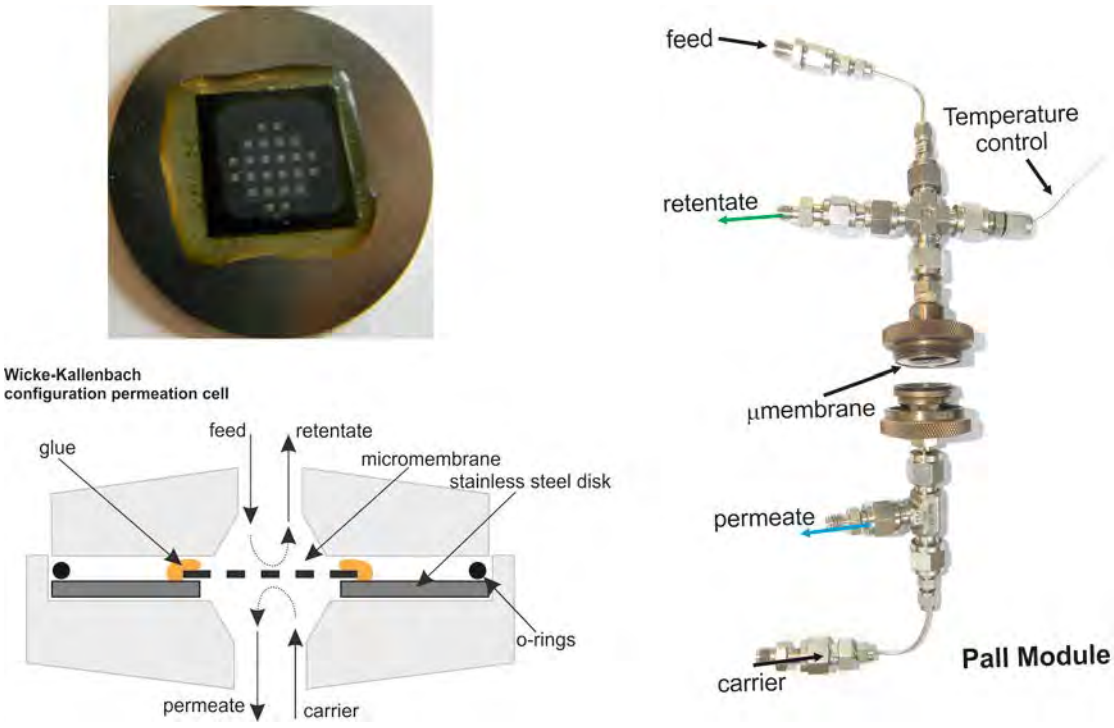

Figure 5. Type C design SIL-1/Si_3N_x micromembrane chip glued over SS disk set up used for gas tightness tests, activation by ozonization (left) and permeation measurements (right).

Table 1 summarizes the main characteristics of the membranes prepared and the results obtained from the integrity tests for SIL-1/Si_3N_x micromembranes and also for their free standing counterparts before template removal. The largest self-supported micromembrane that could be successfully fabricated corresponded to type D design, i.e. 290 μm x 290 μm leading to 3.76 mm^2/cm^2 microporous area per chip surface. Similar results have been described in literature [23]. On the other hand, the SIL-1 micromembranes supported on the Si_3N_x grid were successfully released for all the designs used in this work thanks to the structural reinforcement via mechanical interlocking. This could allow to obtain permeable areas as high as 19.9% of the total chip area (type A design). However, while all designs of SIL-1/Si_3N_x micromembranes could be fabricated, it was found that type A membranes were unreliable, often breaking when handling or during permeation tests, and therefore they were discarded.

Table 1. Main characteristics of the SIL-1 micromembranes developed in this work. Includes integrity assessment after the microfabrication process for free standing membranes and for membranes supported on a Si_3N_x grid.

Back Side Design	**Type A**	**Type B**	**Type C**	**Type D**	**Type E**
N: number of micromembranes per chip	1	4	24	44	61
w_m (mm): characteristic dimension of the back side mask	5	2	1	0.83	0.7
w_0 (mm)[1]: Front side characteristic dimension	4.46	1.46	0.46	0.29	0.16
$w_0^2 \cdot N$ (mm^2):nominal permeable area per chip	19.91	8.55	5.13	3.76	1.61
Undamaged self-suppported SIL-1 µmembranes were obtained	**NO**	**NO**	**NO**	**YES**	**YES**
Undamaged SIL-1/Si_3N_x µmembraneswere obtained	**YES**	**YES**	**YES**	**YES**	**YES**
Grid pattern	Circular	Squared	Squared	Squared	Squared
Porosity (ε)[2]	0.57	0.83	0.83	0.83	0.83

[1] $w_0(mm) = w_m(mm) - 2 \cdot z\,(mm) \cdot \cot an\,(54.74)$ where z is the Si wafer thickness.

[2] $\varepsilon = \frac{\text{number of apertures on top side layer} \cdot \text{surface of each aperture}}{\text{total front side area}}$

3.2. SIL-1 micromembranes activation

After fabrication of the SIL-1 and SIL-1/Si_3N_x micromembranes (step A to step D), removal of the organic structure-directing agent (termed SDA, in this case TPAOH) from the MFI framework becomes necessary to release the micropores for permeation. This activaction is performed after stage D of the microfabrication process since chemical etching of SIL-1 is retarded when the template is still on the zeolite pores, thereby increasing the selectivity (rate of etching) of Si vs. SIL-1.

Template removal is commonly carried out by calcination involving temperatures above 723 K. Our supported SIL-1/Si_3N_x micromembranes were clearly damaged by such conventional calcination. As an example, Figure 6 shows the top surface of type C SIL-1/Si_3N_x micromembranes after calcination at 753 K. In our case, the sudden shrinkage of MFI crystals [12-13] results in mechanical stress in the MFI layer due to the opposite thermal behaviour of the silicon nitride support (thermal expansion coefficient mismatch between c oriented MFI crystals, $-2.49 \cdot 10^{-6}$ K^{-1} [31]; and silicon nitride, $3 \cdot 10^{-6}$ K^{-1} [32]). In our case, this stress is mainly released by the formation of cracks due to the relative high membrane

thickness (4 ± 0.5 µm). Extensive crack formation (marked by the arrows in Figure 6) is easily noticeable. These cracks propagate not only between crystals but also within crystals; characteristic feature of well intergrowth thick layers.

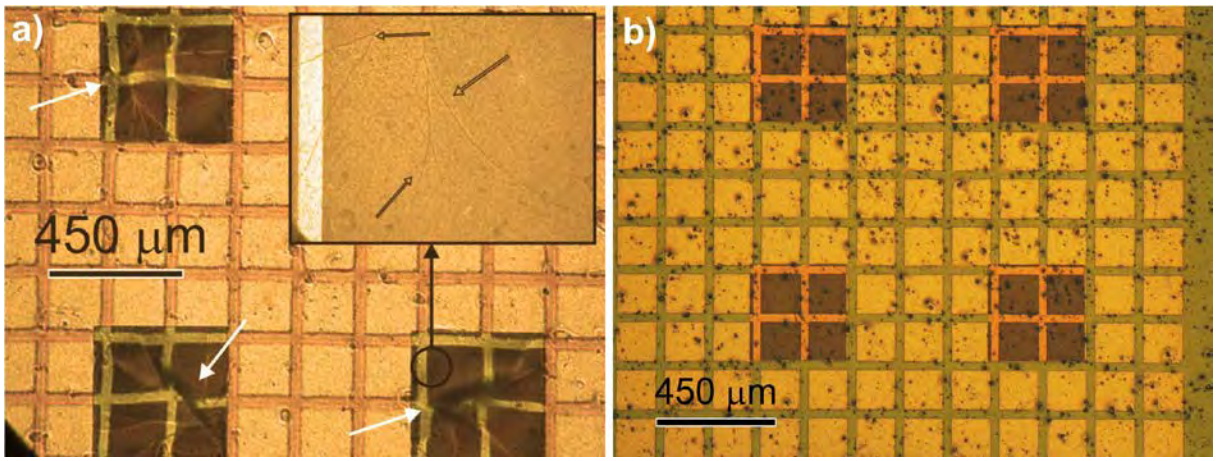

Figure 6. Top view of type C design SIL-1/ Si_3N_x micromembranes after: a) calcination at 753 K for template removal. Inset: propagation of cracks over the micromembrane surface; b) ozone activation process at 473 K.

Thus, the standard calcination procedure was ruled out, and a low temperature ozone activation process [11-12, 33] has been assayed as an alternative method of template removal. In general, ozonization provides highly reactive atomic oxygen and other radical species are able to remove the template from zeolites under mild temperature conditions. To this end, pure O_2 (99.99% Praxair) was fed through an O_3 generator, (Neosyt NEO 500), giving an ozone concentration of approximately 0.15%, and passed over the micromembrane chip previously mounted in the separation set-up (see Figure 5). The temperature was increased at 1 K/min from room temperature to the activation temperature (423 K or 473 K) under dry N_2 (10 sccm) in the feed side and Ar (10 sccm) in the permeate side. The total pressure on both sides of the micromembranes was kept constant at 100 kPa during the activation. The O_2 concentration evolution in the permeate stream was continuously monitored by microGC to monitor the microporous release as template removal was accomplished (see Figure 7). When the desired temperature was attained, the ozone generator was turned on and the feed stream was switched to the O_3/O_2 stream. As can be observed, the O_2 concentration increases gradually with time on stream, in agreement with a controlled SDA release from the micropores. When ozonization was performed at 423 K the micromembranes required more

than 4 h until the O_2 concentration in the permeate was stabilized. On the other hand, less than 1 h was required for SDA removal at 473 K. Since no cracks were observed with the latter procedure, it was selected as the detemplation route in this work. After SDA removal, the SIL-1/Si_3N_x micromembranes were tested for CO_2/H_2 permeation on the same unit.

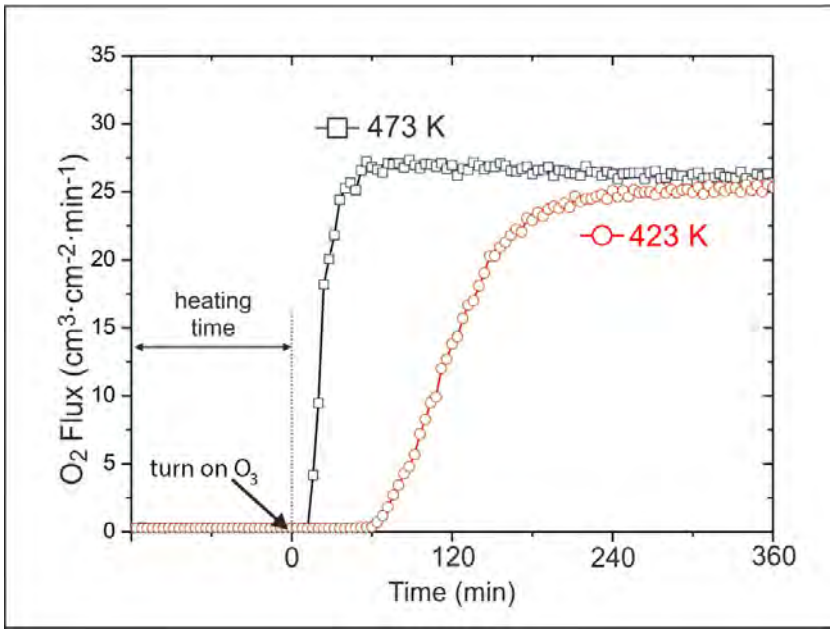

Figure 7. Assessment of template removal from SIL-1/Si_3N_x micromembranes by ozone activation process as a function of temperature.

3.3. CO_2 separation performance

Binary permeation experiments were performed in a continuous flow mode using the set up described in Figure 5, with an equimolar CO_2/H_2 mixture. The separation properties at room temperature for the main SIL-1/Si_3N_x micromembranes with B (1.46 mm characteristic dimension), C (0.46 mm characteristic dimension) and D (0.29 mm characteristic dimension) type designs prepared according to step B procedures 1 and 2 respectively are summarized in Table 2, where both the total permeation molar flow rate (μmol/h) and the permeance ($mol \cdot m^{-2} \cdot s^{-1} \cdot Pa^{-1}$) are reported. The latter was referred to the real permeation area per chip, calculated as $w_0^2 \cdot N \cdot \varepsilon$, where ε is the porosity (free area) left by the underlying Si_3N_x grid. In particular for type D design, three micromembranes prepared following step B procedure 1 and 2 respectively were tested, and the 70% confidence interval was always within ±15% of the average for CO_2 permeation properties. Unfortunately, for the remaining designs there were

not enough samples for any reproducibility assessment. The dissimilar gas separation properties are attributed to the contribution of non selective defects arising during handling, sealing and packaging of the micromembrane chip. In fact, further efforts are focused on "stand alone" robust micromembranes module design to facilitate assembly and testing.

Table 2. Binary CO_2/H_2 permeances and separation factor at room temperature for some of the SIL-1/Si_3N_x micromembranes prepared in this work

	Fabrication Process Back side design (Chip microporosity)/ Step B procedure	Total permeation per chip (μmol/h)		Permeance (10^7 *mol·m^{-2}·s^{-1}·Pa^{-1})		Separation Factor	Knudsen enhancement
NOMENCLATURE		H_2	CO_2	H_2	CO_2	α CO_2/H_2	
DSS_1	D(3.12%)/1	0.46	1.39	27.3	82.7	2.4	11.4
DSS_2	D(3.12%)/1	0.56	1.71	33.5	101	2.4	11.4
DSS_3	D(3.12%)/1	0.76	1.65	45.5	98.0	1.8	8.5
CSS_4	C(4.26%)/1	1.45	3.12	63.0	136	1.8	8.5
BSS_5	B(7.10%)/1	1.61	2.05	41.9	53.5	1.2	5.7
BSS_6	B(7.10%)/1	2.59	2.58	67.6	67.3	0.9	4.2
DSL_7	D(3.12%)/2	0.01	0.14	0.5	8.2	16.9	80.5
DSL_8	D(3.12%)/2	0.03	0.17	1.6	10.1	5.7	27.2
DSL_9	D(3.12%)/2	0.05	0.19	2.8	11.3	3.6	17.2
CSL_10	C(4.26%)/2	0.32	0.97	14.0	42.2	5.9	28.1

Separation of CO_2 from natural gas (CO_2-CH_4) or exhaust gases (CO_2-N_2) are examples of important industrial separation applications where inorganic membranes can play important roles [9, 34]. The higher quadrupole moment and polarizability of CO_2 versus any of the counterparts is responsible for its higher adsorption strength [37]. Over the last few years, CO_2 separation from synthesis gas with FAU [38], SAPO [39] and MFI zeolite type membranes [28, 40-46] has received increasing attention. More specifically, the separation of CO_2/H_2 binary mixtures at room temperature is governed by an adsorption-diffusion mechanism. The target for CO_2 selective membranes involves a trade-off between adsorption strength and mobility through micropores. For MFI type membranes, high pressure in the feed leads not only to higher CO_2 fluxes but also to a higher separation selectivity due to the near saturation of the zeolite at the retentate side and relatively high CO_2 surface diffusivity in MFI micropores. Thus, selective CO_2 adsorption on silicalite (heat of adsorption for CO_2 is 24.3 kJ/mol vs 5.9 kJ/mol for H_2 [47]) leads to pore blocking by CO_2 to a large extent. As a

consequence, MFI membranes have been found to allow preferential permeation of CO_2 at room temperature. The influence of surface modification by amine groups and cation exchange in MFI membranes to increase CO_2 affinity was extensively studied by Hendlund et al. [40-41]. For surface modification, the methylamine gas interacted with the framework of the zeolite membrane once synthesized, increasing the amount of basic sites and thus the carbon dioxide adsorption capacity. The higher CO_2/H_2 separation factors obtained were 6.5 for ternary mixtures $CO_2/H_2/H_2O$ at 333K [40]. Ion-exchange also led to a remarkable increase in the separation factor (from 1.1 to 6.2) at 295 K for the Ba-exchanged ZSM-5 membrane in presence of 2.1% H_2O in the feed stream due to an effective hydrogen blocking by water retained in the pores [41]. The relative high CO_2 permeance values (i.e. $13 \cdot 10^{-7}$ $mol \cdot m^{-2} \cdot s^{-1} \cdot Pa$) were attributed to the high solubility of CO_2 in water and its stronger adsorption in the Ba modified zeolite. Recently, NaY type zeolite membranes have been identified as the most adequate for CO_2/H_2 separation according to Configurational-Bias Monte Carlo (CBMC) simulations along with Molecular Dynamics (MD) [37], due to: i) the improved electrostatic interactions of CO_2 with exchange cations; and, ii) the framework topology. The same authors found for MFI zeolite the simulated CO_2/H_2 permeation selectivities and CO_2 permeabilities at 1 MPa and 300 K to be 10 and 10^5 Barrer, respectively.

The CO_2/H_2 separation properties of the SIL-1/Si_3N_x micromembranes integrated on chip prepared in this work follow the general trends that could be expected from the literature. Figure 8 shows the binary CO_2/H_2 permeances as a function of temperature for type D SIL-1/Si_3N_x micromembranes fabricated using procedure 2 (i.e. extended RIE for the underneath Si), while similar results were obtained for other membranes. It can be seen that CO_2 permeance decreases with temperature throughout the interval studied, as the amount of CO_2 adsorbed in the zeolite pores decreased. At the same time, the H_2 permeance values increased by a factor of 2 from 278 K up to 473 K due to the combined effect of the increased diffusion rate for H_2 (activated permeation) and the decrease of CO_2 occupancy that releases more pore space for H_2 permeation. This indicates that the increase in CO_2 diffusion rate with temperature is not enough to compensate the decrease in CO_2 surface coverage. A very similar behaviour was previously reported for the permeation behaviour of CO_2/N_2 mixtures in conventional MFI membranes [28]. Figure 8 also presents the Knudsen enhancement factor calculated as the ratio between the experimentally observed separation factor and the Knudsen CO_2/H_2separation factor, ($\sqrt{2}/44 = 0.21$). The Knudsen enhancement decreases from 28 at

278 K, where CO_2 adsorption is governing the separation mechanism, to around 4 at 473 K, where most of the observed permeation can be explained as a result of activated diffusion through micropores.

Among the 10 SIL-1/Si_3N_x micromembranes in table 2, six were fabricated according to RIE (step B) procedure 1 and four following procedure 2. With the exception of BS_6, that presents the lower separation factor, all the samples exhibit higher permeances for CO_2. For a given procedure (i.e. set of RIE-microfabrication conditions), the registered CO_2, H_2 binary permeances depicted in Figure 8 depend on the mask design used, (i.e. the front side characteristic dimension ranging from 1.46 mm in type B design to 0.29 mm for type D design). For a longer characteristic dimension, the H_2 permeance increases and the CO_2/H_2 separation factor decreases, suggesting a higher concentration of defects. This is in agreement with the expectation that larger unsupported membrane surfaces are more likely to present defects (i.e. intercrystalline grain boundaries and pinholes) that serve as non-zeolitic permeation paths. These defects, likely a few nm in size, are nevertheless much larger than the subnanometric pores of the zeolite (≈ 0.55 nm for MFI), thereby increasing permeation flux and decreasing selectivity.

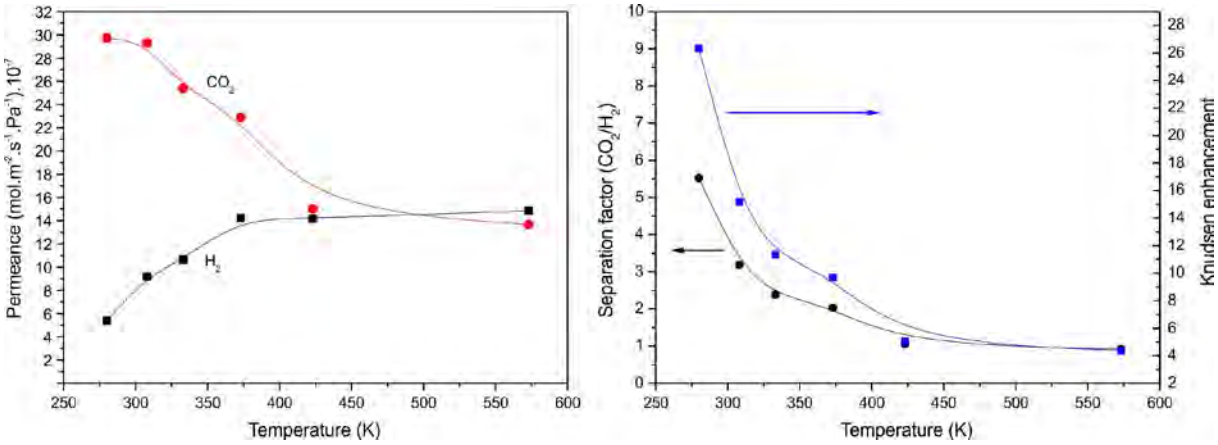

Figure 8. Binary CO_2/H_2 permeances (left); separation factor, and Knudsen enhancement factor (right) as a function of temperature for type D design SIL-1/Si_3N_x micromembrane.

It is interesting to note that, RIE conditions used seem to be the dominant influence on their permeation properties independently on the SIL-1/Si_3N_x micromembrane design. The morphology of the membranes obtained for RIE Procedures 1 and 2 respectively, are schematically shown in Figure 9, together with SEM analyses of top surfaces and cross sections. SEM images after extended RIE 2 procedure reveals the existence of terraces 4

microns depth. Moreover, the morphology of the MFI layer over the terrace edges is different from the observed on the plain terrace. This effect could be explained by the nutrients inhibited access to the bottom edges with hydrothermal synthesis time. In spite of this, all the as prepared micromembranes are able to mimic the underlying microstructure. Procedure 2 clearly leads to membranes with lower permeance values and higher CO_2/H_2 separation factors, indicative of lower concentration of defects, compared to membranes prepared with procedure 1. This experimental observation could be explained on the basis of membrane softening by corrugation effect provoked by the terraces. Corrugated diaphragms are widely used for some specific MEMS devices (i.e. microphones, mechanical decouplers...) to reduce the effects of the residual stress [47-48] compared to flat counterparts. The most distinguished features of corrugated membranes are: higher mechanical sensitivity, enhanced uniformity of pressurized deformations, extended range for linear deflection under applied pressure, to name a few. By analogy, the SIL-1/Si_3N_x micromembranes prepared according to extended RIE procedure 2 are preferred over standard RIE counterparts because procedure 2 provides with a more uniform distribution of residual stresses leading to a lower number of defects. The resulting mechanical stresses imposed on the MFI layer for Procedure 1 samples could be eventually released locally via crack formation and easily propagated over the top surface. On the contrary, for Procedure 2, the deeper RIE etching alleviates the local microstructural tensions on the surface; and finally, allows decoupling the mechanical stresses at the terrace avoiding crack propagation.

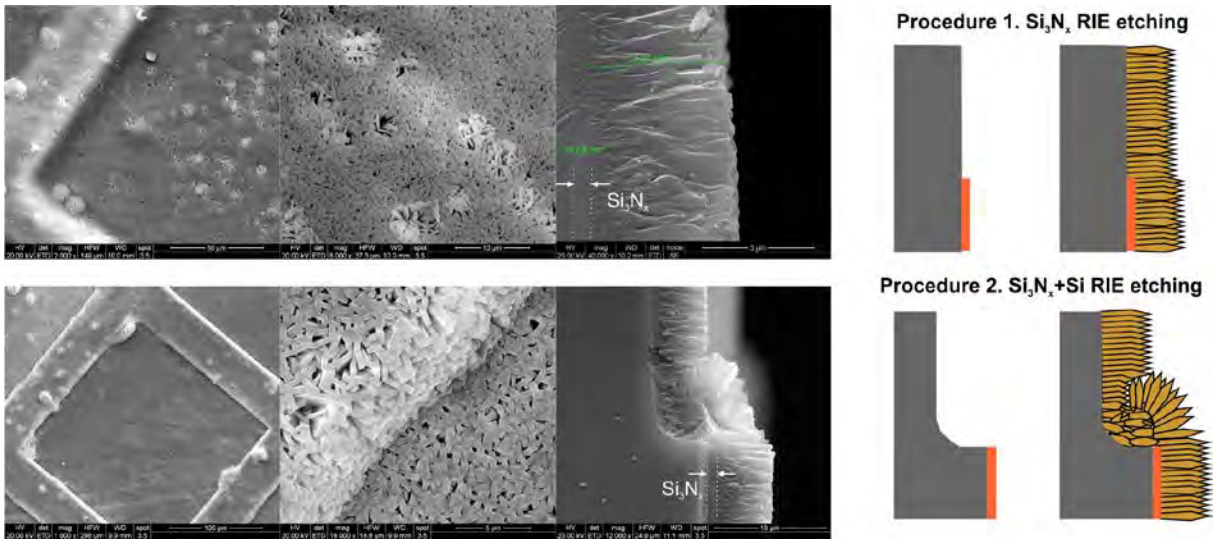

Figure 9. SEM observations of top surfaces and cross sections of type D design membranes prepared according to Procedure 1, DSS_2 (top) and Procedure 2, DSL_7 (bottom).

Figure 10 represents CO_2/H_2 separation factors against CO_2 permeability (expressed in Barrer) for MFI zeolite membranes, including the available literature data and the results obtained with the SIL-1/Si_3N_x micromembranes used in this work (see Table 3). CO_2-selective polymeric membranes have been also included for comparison purposes. Rubbery polymeric membranes, such as poly(dimethylsiloxane) (PDMS) and poly(1-trimethylsilyl-1-propyne) (PTMSP), typically exhibit solubility selectivity towards CO_2 and diffusivity selectivity towards H_2 [51]. CO_2 permeability values of 3200 and 18200 barrer have been described for PDMS and PTMPS respectively for synthetic syngas at the expense of low CO_2/H_2 selectivity (below 3.5 at 35ºC). Further improvement on CO_2 selectivity may be achieved by means of polymers with polar groups to harness CO_2 interactions. Thus, pure CO_2/H_2 gas selectivity values around 12 with a CO_2 permeability of 570 barrer at 35ºC and 1 atm as driving force have been reported for cross linked poly(ethylene glycol)acrylate (XLPEO) containing branches with methoxy groups [52]. It should be noted that these data have been obtained for short time exposure where plasticization effects are negligible, and the separation performance over long periods still needs to be substantiated.

As can be observed, the best performance in terms of separation factor/permeance correspond to the SIL-1/Si_3N_x micromembranes prepared using extended RIE (procedure 2) that gave rise to a lower concentration of defects and hence to larger CO_2 separation factors. The best results were obtained for DSL_7, with a CO_2/H_2 separation factor of 16.9 at a CO_2 permeance of $6.8 \cdot 10^{-7}$ $mol \cdot m^{-2} \cdot s^{-1} \cdot Pa^{-1}$ both measured at ambient conditions. Analogous results have been attained for Stainless-steel net-imbedded silicalite-1 membranes [44] prepared by secondary growth over 3 days at 170ºC. Similar separation factor was also reported by Hedlund [42] for SIL-1 membranes on alumina disks, although with a considerably higher permeation flux. This was made possible by an elaborate preparation procedure that included pore masking and seeding under clean room conditions. This procedure avoided penetration of the zeolite seeds into the alumina support pores, reducing the resistance of the support and allowing the development of a very thin membrane (0.7 μm). A CO_2/H_2 separation factor of 16.2 at a CO_2 permeance of $8.0 \cdot 10^{-6}$ $mol \cdot m^{-2} \cdot s^{-1} \cdot Pa^{-1}$ were obtained.

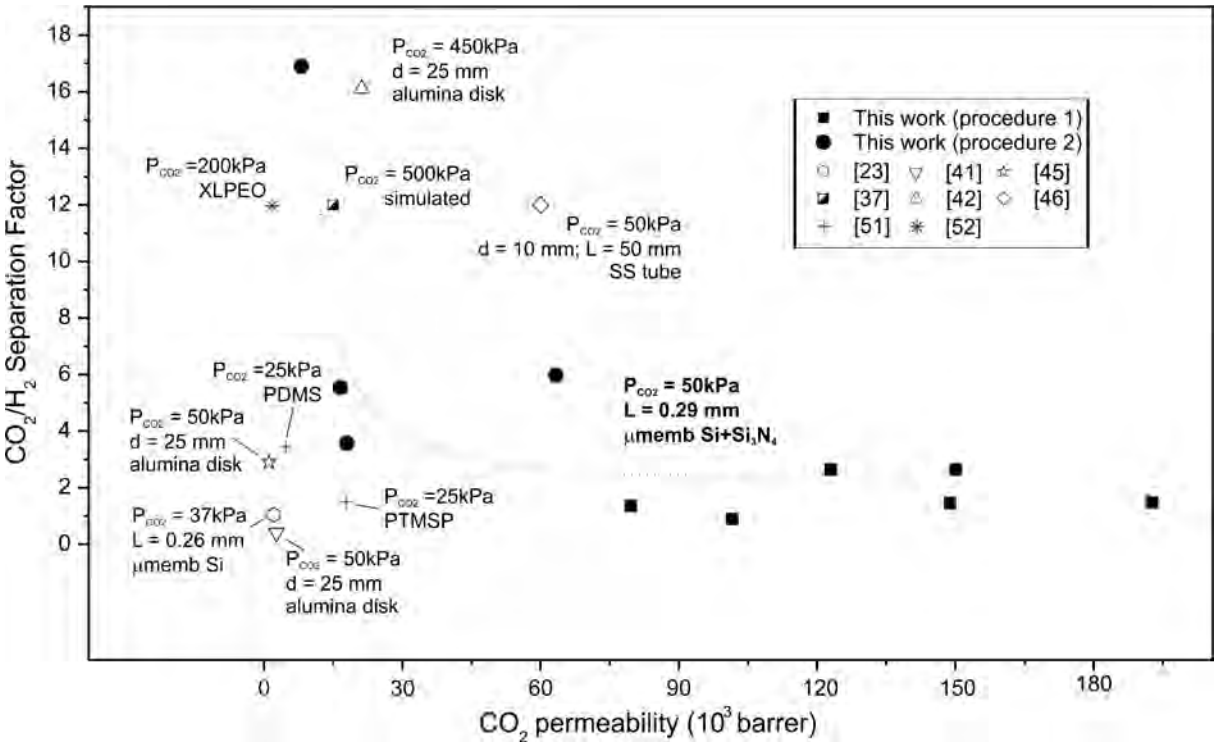

Figure 10. CO_2/H_2 separation factor vs. CO_2 permeability. Comparison between the data obtained with the SIL-1/Si_3N_x micromembranes prepared in this work and published results with MFI type membranes and micromembranes (see Table 3 for details concerning literature data) and polymeric counterparts ([51-52]).

Regarding micromembranes (or on-chip membranes), the results presented here clearly outperform those described by Yeung et al [23] for free standing SIL-1 and ZSM-5 (Si/Al= 40) micromembranes grown over Si wafers with 3.06 $mm^2$of microporous membrane area. These authors observed that the H_2-CH_4-CO_2 separation behaviour depended strongly on the Si/Al ratio of the zeolite framework which was attributed to differences on the acid-base Lewis properties. Thus, micromembranes with lower Si/Al ratio (Si/Al = 40) were moderately selective for hydrogen permeation, (CO_2/H_2 separation factor = 0.6). On the other hand, CH_4 and CO_2 permeated preferentially through SIL-1 micromembranes (Si/Al = ∞), exhibiting CO_2/H_2 separation factors around 1.5. The main structural difference between the membranes prepared in this work and those of Yeung is that our SIL-1 micromembranes have been grown over Si_3N_x microsieves [19, 50]. This is expected to give a higher mechanical resistance to the zeolite micromembranes, and indeed the improved separation performance suggests a lower concentration of defects. However, in addition to increased resilience, the Si_3N_x

support grid may also affect the chemical composition of the synthesized membranes, with direct consequences on separation performance. This hypothesis is discussed next.

In the past, high CO_2/H_2 separation factors observed for SIL-1 membranes on alumina and stainless steel supports have been attributed to the presence of Al^{3+} and Fe^{3+} species in the film. Their presence is ascribed to the harsh synthesis conditions that promote partial dissolution of the support, releasing Al^{3+} or Fe^{3+} cations that may be incorporated into the growing zeolite film, resulting in a membrane with more affinity towards CO_2. The same mechanism is likely to operate with our SIL-1 micromembranes synthesized over Si_3N_x supports: some dissolution is likely to take place given the reaction conditions used and times involved (3 days, pH=11, 130°C), facilitating the incorporation of nitrogen in the zeolite framework, where some Si-O-Si links would become Si-NH-Si [53-54]. Since lone pairs of electrons on surface nitrogen groups can act as active Lewis base sites, nitrided zeolites would exhibit a more basic behaviour enhancing the affinity towards the acidic CO_2. As a matter of fact, mesoporous silicon nitrides characterized by high CO_2 adsorption capacity even at 373K, have been recently proposed for reversible CO_2 capture [55]. To confirm such hypothesis, CO_2 temperature programmed desorption experiments (AUTOCHEM II Micromeritics) were performed on SIL-1/Si_3N_x micromembranes and on their free standing (N-free) SIL-1 counterparts grown on bare Si microchips. After CO_2 saturation at 243K, the thermograms shown in Figure 11 were obtained. In both samples, two CO_2 desorption peaks are clearly identified. However, for the micromembranes grown on Si_3N_x microsieves both desorption peaks shift noticeably towards higher temperature, from 262K to 264K; and from 287K to 302K respectively. Particularly, the more strongly adsorbed component (i.e. the CO_2 desorption event that occurs above 273K) is deemed responsible for the CO_2/H_2 separaration properties claimed in this work, and the fact that it now appears at a temperature 15 degrees higher is a clear indication of increased adsorption strength for the N-containing zeolites. In this way, the higher CO_2/H_2 separation factors compared to previous works on Si wafers [23] can be explained as a result of a stronger CO_2 interaction for SIL-1 micromembranes grown on Si_3N_x microsieves and are likely due to the incorporation of N in the zeolite framework.

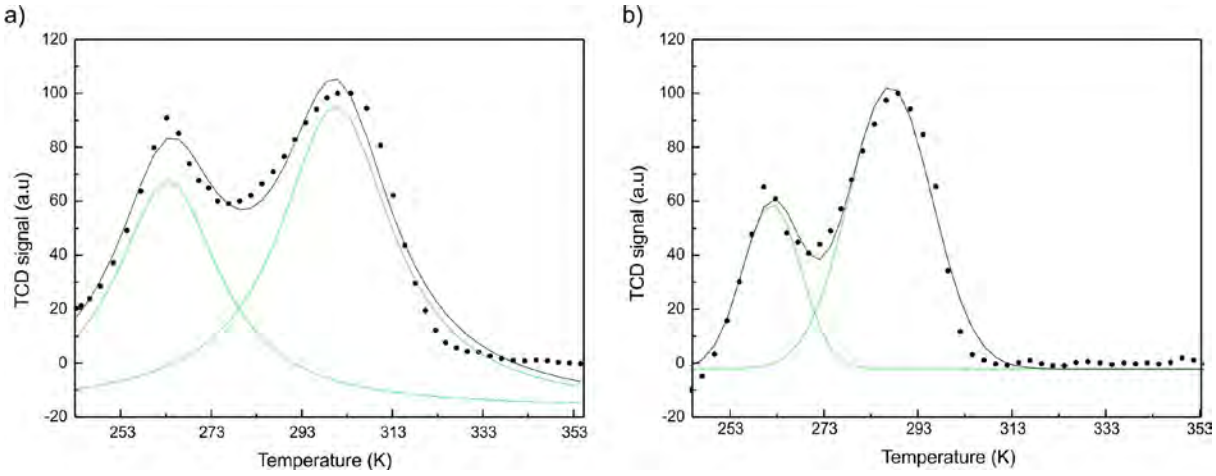

Figure 11. CO_2 TPD analyses for DSL_7 SIL-1/Si_3N_x micromembrane a), and free standing SIL-1 micromembrane grown on Si wafers (b).

Table 3. CO_2/H_2 separation performance with MFI zeolite membranes at room temperature.

Reference	This work DSL_7	This work DSL_8	[23]	[23]	[42]	[41]	[45]	[46]	[44]
Feed Composition	CO_2/H_2 50/50	CO_2/H_2 50/50	$H_2/CH_4/CO_2$ 62/12/26	$H_2/CH_4/CO_2$ 62/12/26	CO_2/H_2 50/50	CO_2/H_2 50/50	CO_2/H_2 50/50	CO_2/H_2 50/50	CO_2/H_2 50/50
CO_2/H_2 Separation factor	16.9	5.7	1.5	0.6	16.2	0.64	2.9	12	16.8
Permeance (10^{-7}· mol·s^{-1}·m^{-2}·Pa^{-1})	CO_2 6.8	CO_2 8.4	CO_2 1.6	CO_2 0.7	CO_2 80	CO_2 19.2	CO_2 1.8	CO_2 3.6	CO_2 7
	H_2 0.4	H_2 1.3	H_2 5.1	H_2 2.2	H_2 5	H_2 30	H_2 0.6	H_2 0.3	H_2 0.4
Membrane Dimension (mm)	L=0.29	L=0.29	L=0.26	L=0.26	Ø=25	Ø=25	Ø=25	Ø=10 L=50	n.a.
Experimental Permeation Conditions (*)	Sweep gas (Ar) ΔP=0	Sweep gas (Ar) ΔP=0	ΔP=41 kPa	ΔP=41 kPa	ΔP=800 kPa	Sweep gas (He) ΔP= 90 kPa	Sweep gas (He) ΔP=0	Sweep gas (He) ΔP=0	Sweep gas (Ar) ΔP=0
Zeolite	SIL-1	SIL-1	SIL-1	ZSM-5 Si/Al 40	SIL-1	SIL-1	SIL-1	SIL-1	SIL-1
Zeolite Thickness (µm)	4.5	4.5	5	5	0.7	0.5	2	50	n.a.
Support	**Si_3N_x**		**Si**		**Alumina Disc**			**Tubular SS**	**Net SS**
	µMembrane								

4. Conclusions

On chip SIL-1 micromembranes have been successfully synthesized on customized Si_3N_x microsieves by following 4 step microfabrication process. In particular, two different micromembrane systems are obtained by tuning RIE conditions of microfabrication step B devoted to Si_3N_x microsieve definition. In both systems, the homogenous SIL-1 layers, 4 microns thick, follow the underlying microstructure. Nominal permeable areas as high as 19.9% of the total chip area (type A design) have been obtained thanks to the structural reinforcement via mechanical interlocking at the SIL-1/Si_3N_x interface. The controlled SDA release from micropores by ozone detemplation at 473K alleviates the mechanical stress imposed on the zeolite layer. Thus, SIL-1/Si_3N_x micromembranes with permeation areas as high as 8.5% of the total chip area (type B design) have been successfully released, mounted and tested for CO_2 separation. The CO_2/H_2 separation properties of the micromembranes integrated on chip follow the typical trend for adsorption-diffusion governing mechanism. Nearly all the samples exhibit higher permeances for CO_2. However, as it was expected, H_2 permeance increases along the characteristic dimension of the micromembrane due to the higher contribution of grain boundary defects. Extended RIE conditions used for samples prepared by Procedure 2 can determine the CO_2 separation performance, because the existence of terraces 4 microns depth provides with a more uniform distribution of residual stresses leading to a lower number of defects. In addition to increased resilience, the Si_3N_x microsieve is also affecting the chemical composition of the synthesized SIL-1 layer, and consequently its CO_2 adsorption properties. As a result, SIL-1/Si_3N_x micromembranes integrated on chip with 3.12% as permeable area with 8.7 as average CO_2/H_2 separation factor and 11785 Barrer for CO_2 permeability have been attained. The most outstanding micromembrane chip among those tested is DSL_7 with a CO_2/H_2 separation factor of 16.9 at a CO_2 permeability of 9800 Barrer at ambient conditions. These are encouraging results that may lead to improved fabrication procedures to prepare self-standing membranes. However, only one sample out of 10 prepared in this work (table 2) achieved this performance. Further research is needed to obtain reliable membrane statistics and to improve the reproducibility of the microfabricated membranes.

Acknowledgements

Financial support from Gobierno de Aragón, NanoAracat, and MICINN-MINECO, Spain, is gratefully acknowledged.

References

[1] K.F. Jensen, Silicon-Based Microchemical Systems: Characteristics and Applications, MRS Bulletin 31 (2006) 101-107.

[2] C.J.M. Van Rijn, Nanotechnology and Nano Engineered Membranes (chapter. 9), in: C.J.M. Van Rijn (Eds.), Nano and Micro Engineered Membrane Technology (vol. 10), Membrane Science and Technology Series, Elsevier B.V., Amsterdam, 2004, 277-333.

[3] A.J. Franz, K.F. Jensen, M.A. Schmidt, S. Firebaugh, U.S. Patent No. 6,541,676. Washington, DC: U.S. Patent and Trademark Office, 2003.

[4] B.A. Wilhite, M.A. Schmidt, K.F. Jensen, Palladium-based micromembranes for hydrogen separation: Device performance and chemical stability, Industrial and Engineering Chemistry Research 43(22) (2004) 7083-7091.

[5] H.D. Tong, F.C. Gielens, J.G.E. Gardeniers, H.V. Jansen, J.W. Berenschot, M.J. de Boer, J.H. de Boer, C.J.M. Van Rijn, M.C. Elwenspoek, Microsieve supporting palladium-silver alloy membrane and application to hydrogen separation, Journal of Microelectromechanical Systems. 14(1) (2005) 113-124.

[6] H.D. Tong, F.C. Gielens, J.G.E. Gardeniers, H.V. Jansen, J.W. Berenschot, M.J. de Boer, J.H. de Boer, C.J.M. Van Rijn, M.C. Elwenspoek, Microsieve supporting palladium-silver alloy membrane and application to hydrogen separation, Journal of Microelectromechanical Systems 14(1) (2005) 113-124.

[7] J. Coronas, J. Santamaria. The use of zeolite films in small-scale and micro-scale applications. Chemical Engineering Science 59 (22-23) 4879-4885.

[8] M.P. Pina, R. Mallada, M. Arruebo, M. Urbiztondo, N. Navascués, O. de la Iglesia, J. Santamaria, Zeolite films and membranes. Emerging applications, Microporous and Mesoporous Materials 144 (2011) 19-27.

[9] M. Arruebo, R. Mallada, M.P. Pina, Developments in zeolite membrane applications, in: A.K. Pabby, S.S.H. Riziv, A.M. Sastre (Eds.), Handbook of Membrane Separations, CRC Press., 2013, 269-323.

[10] Y.S. Lin, M.C. Duke, Recent progress in polycrystalline zeolite membrane research, Current Opinion in Chemical Engineering 2 (2013) 209-216.

[11] E.R. Geus, H. van Bekkum, Calcination of large MFI-type single crystals, Part 2: Crack formation and thermomechanical properties in view of the preparation of zeolite membranes, Zeolites 15(4) (1995) 333-341.

[12] J. Dong, Y.S. Lin, M.Z.C. Hu, R.A. Peascoe, E.A. Payzant, Template-removal-associated microstructural development of porous-ceramic-supported MFI zeolite membranes, Microporous and Mesoporous Materials 34(3) (2000) 241-253.

[13] H-K. Jeong, Z. Lai, M. Tsaptsis, J.C. Hanson, Strain of MFI crystals in membranes: An in situ synchrotron X-ray study, Microporous and Mesoporous Materials 84 (2005) 332-337.

[14] J. Choi, H.K. Jeong, M.A. Snyder, J.A. Stoeger, R.I. Masel, M. Tsapatsis, Grain boundary defect elimination in a zeolite membrane by rapid thermal processing, Science 325 (2009) 590-593.

[15] T. Lee, J. Choi, M. Tsapatsis, On the performance of c-oriented MFI zeolite membranes treated by rapid thermal processing, Journal of Membrane Science 436 (2013) 79-89.

[16] S.K. Wirawan, D. Creaser, J. Lindmark, J. Hedlund, I.M. Bendiyasa, W.B. Sediawan, H_2/CO_2 permeation through a silicalite-1 composite membrane, Journal of Membrane Science 375(1-2) (2011) 313-322.

[17] E. Mateo, R. Lahoz, G.F. de la Fuente, A. Paniagua, J. Coronas, J. Santamaria, Preparation of silicalite-1 micromembranes on laser-perforated stainless steel sheets, Chemistry of Materials 16(24) (2004) 4847-4850.

[18] E. Mateo, R. Lahoz, G.F. de la Fuente, A. Paniagua, J. Coronas, J. Santamaría, Preparation and application of silicalite-1 micromembranes on laser-perforated stainless steel sheets, Journal of Membrane Science 316(1-2) (2008) 28-34.

[19] M.J. den Exter, H. van Bekkum, C.J.M. Rijn, F. Kapteijn, J.A. Moulijn, H. Schellevis, C.I.N. Beenakker, Stability of oriented silicalite -1 films in view of zeolite membrane preparation, Zeolites 19(1) (1997) 13-20.

[20] Y.S.S. Wan, J.L.H. Chau, A. Gavriilidis, K.L. Yeung, Design and fabrication of zeolite-based microreactors and membrane microseparators, Microporous and Mesoporous Materials 42(2-3) (2001) 157-175.

[21] J.L.H. Chau, Y.S.S. Wan, A. Gavriilidis, K.L. Yeung, Incorporating zeolites in microchemical systems, Chemical Engineering Journal 88(1-3) (2002) 187-200.

[22] J.L.H. Chau, A.Y.L. Leung, K.L. Yeung, Zeolite micromembranes, Lab on a Chip 3(2) (2003) 53-55.

[23] Y.L.A. Leung, K.L. Yeung, Microfabricated ZSM-5 zeolite micromembranes, Chemical Engineering Science 59(22-23) (2004) 4809-4817.

[24] S.M. Kwan, Y.L.A. Leung, K.L. Yeung, Gas permeation and separation in ZSM-5 micromembranes, Separation and Purification Technology 73 (2010) 44-50.

[25] S. Mintova, T. Bein, Microporous films prepared by spin-coating stable colloidal suspensions of zeolites, Adv. Mater. 13 (2001a) 1880-1883.

[26] I. Pellejero, M. Urbiztondo, M. Villarroya, J. Sesé, M.P. Pina, J. Santamaría, Development of etching processes for the micropatterning of silicalite films, Microporous and Mesoporous Materials 114(1-3) (2008) 110-120.

[27] I. Pellejero, J. Agustí, M.A. Urbiztondo, J. Sesé, M.P. Pina, J. Santamaría, G. Abadal, Nanoporous Silicalite-only Cantilevers as Micromechanical Sensors: fabrication, resonance response and VOCs sensing performance, Sensors and Actuators B: Chemical 168 (2012) 74-82.

[28] M.P. Bernal, J. Coronas, M. Menéndez, J. Santamaría, Separation of CO2/N2 mixtures using MFI type zeolite membranes, AIChE J. 50 (2004) 127-35.

[29] I. Lee, J.L. Buday, H-K Jeong, □-Tiles and mortar approach: A simple technique for the facile fabrication of continuous b-oriented MFI silicalite-1 thin films, Microporous and Mesoporous Materials 122 (2009) 288–293.

[30] E. Kim, J. Choi, M. Tsapatsis, On defects in highly a-oriented MFI membranes, Microporous and Mesoporous Materials 170 (2013) 1–8.

[31] D.S. Bhange, V. Ramaswamy, High temperature thermal expansion behavior of silicalite-1 molecular sieve: in situ HTXRD study, Microporous and Mesoporous Materials 103(1-3) (2007) 235-242.

[32] http://www.vaxasoftware.com/doc_edu/fis/coefidilat.pdf (Accessed July 2013).

[33] S. Heng, P.P.S. Lau, K.L. Yeung, M. Djafer, J.-C. Schrotter, Low-temperature ozone treatment for organic template removal from zeolite membrane, Journal of Membrane Science 243(1-2) (2004) 69-78.

[34] V. Sebastián, I. Kumakiri, R. Bredesen, M. Menéndez, Zeolite membranes for CO2 removal: Operating at high pressure, Journal of Membrane Science 192 (2007) 92-97.

[35] J. Caro, M. Noack, Zeolite membranes - Recent developments and progress, Microporous and Mesoporous Materials 115 (2008) 215-233.

[36] L. Zhang, I.S. Park, K. Shqau, W.S.W. Ho, H. Verweij, Supported inorganic membranes: promises and challenges, Journal of Membrane Science 61(4) (2009) 61-71.

[37] R. Krishna, J.M. van Baten, In silico screening of zeolite membranes for CO2 capture, Journal of Membrane Science 360 (2010) 323–333.

[38] K. Kusakabe, T. Kuroda, K. Uchino, Y. Hasegawa, S. Morooka, Gas permeation properties of ion-exchanged faujasite-type zeolite membranes, AIChE J 45(6) (1999) 1220-1226.

[39] M. Hong, S. Li, J.L. Falconer, R.D. Noble, Hydrogen purification using a SAPO-34 membrane, Journal of Membrane Science 307 (2008) 277-283.

[40] J. Lindmark, J. Hedlund, Modification of MFI membranes with amine groups for enhanced CO_2 selectivity, Journal of Materials Chemistry 20 (2010) 2219-2225.

[41] J. Lindmark, J. Hedlund, Carbon dioxide removal from synthesis gas using MFI membranes, Journal of Membrane Science 360(1-2) (2010) 284-291.

[42] L. Sandström, E. Sjöberg, J. Hedlund, Very high flux MFI membrane for CO2 separation, Journal of Membrane Science 380(1-2) (2011) 232-240.

[43] A. Alshebami, M. Pera-Titus, E. Landrivon, Th. Schiestel, S. Miachon, J.A. Dalmon, Nanocomposite MFI-Ceramic hollow fibers: prospects for CO_2 separation, Microporous and Mesoporous Materials 115 (2008) 197-205.

[44] H. Guo, G. Zhu, H. Li, X. Zou, X. Yin, W. Yang, S. Qiu, R. Xu, Hierarchical growth of large-scale ordered zeolite silicalite-1 membranes with high permeability and selectivity for recycling CO2, Angew. Chem. Int. Ed. 42 (2006) 7053-7056.

[45] X. Gu, Z. Tang, J. Dong, On-stream modification of MFI zeolite membranes for enhancing hydrogen separation at high temperature, Microporous and Mesoporous Materials 111(1-3) (2008) 441-448.

[46] W.J.W. Bakker, F. Kapteijn, J. Poppe, J.A. Moulijn, Permeation characteristics of a metal-supported silicalite-1 zeolite membrane, Journal of Membrane Science 117(1-2) (1996) 57-78.

[47] S.K. Wirawan, M. Peterson, D. Creaser, Adsorption of CO, CO_2 and H_2 in silicalite-1: measurements and simulations, AIChE J. 8(1) (2008) 9-19.

[48] Q. Zou, Z. Li, L. Liu, Theoretical and experimental studies of single-chip-processed miniature silicon condenser microphone with corrugated diaphragm, Sensors and Actuators A 63 (1997) 209-215.

[49] R.M. Lin, W.J. Wang, Structural dynamics of Microsystems-current state of research and future developments, Mechanical Systems and Signal Processing 20 (2006) 1015-1043.

[50] C.J.M. van Rijn, M.C. Elwenspoek, Micro filtration membrane sieve with silicon micromachining for industrial and biomedical applications, IEEE proc. MEMS (1995) 83-87.

[51] T.C. Merkel, R.P. Gupta, B.S. Turk, B.D. Freeman, Mixed-gas permeation of syngas components in poly(dimethylsiloxane) and poly(1-trimethylsilyl-1-propyne) at elevated temperatures, Journal of Membrane Science 191 (2001) 85-94.

[52] H. Lin, B.D. Freeman, Materials selection guidelines for membranes that remove CO2 from gas mixtures. Journal of Molecular Structure 739 (2005) 57–74.

[53] K.D. Hammond, S.M. Auerbach, Modeling the structure and spectroscopy of alkaline zeolites, in: Silica and Silicates in Modern Catalysis, Journal of Catalysis 269(1) (2010) 53–63.

[54] V. Agarwala, G.W. Hubera, M. Curtis Conner, S.M. Auerbach, Kinetic stability of nitrogen-substituted sites in HY and silicalite from first principles, Journal of Catalysis 270(2) (2010) 249–255.

[55] H. Yang, A.M. Khan, Y. Yuan, S.C. Tsang, Mesoporous Silicon Nitride for Reversible CO_2 Capture, Chemistry Asian Journal 7(3) (2012) 498-502.

Figure caption

Figure 1. General fabrication scheme for reinforced SIL-1 micromembranes over Si_3N_x microsieves.

Figure 2. General top view of the different SIL-1/Si_3N_x micromembrane designs patterned on a 3" Si wafer.

Figure 3.A. Back side view for the SIL-1 micromembranes prepared in this work: type D design (a); type C design (b); close up view of the back for samples prepared according to Step B procedure 1: square shaped Si_3N_x grid (c); and circular Si_3N_x grid (d).

Figure 3.B. Top and cross section views for the SIL-1 micromembranes prepared in this work: type D design (e); close up view of the top surface (f); cross section view for samples prepared according to Step B: procedure 1. (g); and procedure 2. (h).

Figure 4. XRD analyses for the SIL-1/Si_3N_x micromembranes prepared in this work.

Figure 5. Type C design SIL-1/Si_3N_x micromembrane chip glued over SS disk set up used for gas tightness tests, activation by ozonization (left) and permeation measurements (right).

Figure 6. Top view of type C design SIL-1/ Si_3N_x micromembranes after: a) calcination at 753 K for template removal. Inset: propagation of cracks over the micromembrane surface; b) ozone activation process at 473 K. .

Figure 7. Assessment of template removal from SIL-1/Si_3N_x micromembranes by ozone activation process as a function of temperature.

Figure 8. Binary CO_2/H_2 permeances (left); separation factor, and Knudsen enhancement factor (right) as a function of temperature for type D design SIL-1/Si_3N_x micromembranes.

Figure 9. SEM observations of top surfaces and cross sections of type D design membranes prepared according to Procedure 1, DSS_2 (top) and Procedure 2, DSL_7 (bottom).

Figure 10. CO_2/H_2 separation factor vs. CO_2 permeability. Comparison between the data obtained with the SIL-1/Si_3N_x micromembranes prepared in this work and published results with MFI type membranes and micromembranes (see Table 3 for details concerning literature data) and polymeric counterparts ([51-52]).

Figure 11. CO_2 TPD analyses for DSL_7 SIL-1/Si_3N_x micromembrane a), and free standing SIL-1 micromembrane grown on Si wafers (b).

Table List